# Deformation of Microchannels Embedded in an Elastic Medium

**Vivek Ramachandran**[1]
Integrated Soft Materials Laboratory,
Carnegie Mellon University,
Pittsburgh, PA 15213
e-mail: vivek.ramachandran@epfl.ch

**Carmel Majidi**[2]
Integrated Soft Materials Laboratory,
Carnegie Mellon University,
Pittsburgh, PA 15213
e-mail: cmajidi@andrew.cmu.edu

*The deformation of microfluidic channels in a soft elastic medium has a central role in the operation of lab-on-a-chip devices, fluidic soft robots, liquid metal (LM) electronics, and other emerging soft-matter technologies. Understanding the influence of mechanical load on changes in channel cross section is essential for designing systems that either avoid channel collapse or exploit such collapse to control fluid flow and connectivity. In this paper, we examine the deformation of microchannel cross sections under far-field compressive stress and derive a "gauge factor" that relates externally applied pressure with change in cross-sectional area. We treat the surrounding elastomer as a Hookean solid and use two-dimensional plane strain elasticity, which has previously been shown to predict microchannel deformations that are in good agreement with experimental measurements. Numerical solutions to the governing Lamé (Navier) equations are found to match both the analytic solutions obtained from a complex stress function and closed-form algebraic approximations based on linear superposition. The application of this theory to soft microfluidics is demonstrated for several representative channel geometries.*
[DOI: 10.1115/1.4040477]



## 1 Introduction

Microfluidic systems for lab-on-a-chip diagnostics, biomaterials printing, and pathogen detection have had a transformative impact on medicine and biotechnology [1–4]. These devices are typically composed of microfluidic channels embedded in soft elastic materials and are produced using "soft lithography" fabrication techniques [5–7]. In recent years, *soft microfluidic* architectures have also been used for stretchable electronics with liquid metal (LM) [8–10], organ-on-a-chip tissue engineering [11,12], and fluid-powered soft robotics [13,14]. In most of these applications, the mechanical deformation of the embedded microfluidic channels and surrounding elastic medium are strongly coupled—leading to elasto-mechanical dependencies that can significantly influence device operation. Understanding the mechanics of these interactions is essential for developing predictive modeling tools that can inform the design and operation of soft microfluidic systems.

In many applications, elasto-mechanical coupling is an undesired consequence of using soft materials that can interfere with device functionality or performance. This is particularly true with stretchable electronics that use microfluidic LM wiring for soft, stretchable, and elastic circuits. For these circuits, microchannel deformation typically causes the electrical resistance to increase and can alter the passive electronic properties of the circuit [15]. However, in some cases, elasto-mechanical coupling can be exploited to achieve unique functionalities that are not possible with a rigid device. This includes microfluidic "Quake" valves [16], LM pressure sensors and strain gauges [17–20], fluidic actuation [13,14], and pressure-controlled microfluidics that filter or capture nanoparticles [21,22] (Fig. 1(*a*)). In general, a theoretical model that relates the deformation of the microchannel and surrounding elastomer can inform device operation and enable the system to be designed in a way to either enhance or mitigate this coupling.

This paper presents theories that relate the influence of far-field stress on the deformation of a microchannel embedded within a soft elastic medium (Fig. 1(*b*)). Solutions are obtained for the cross-sectional geometries shown in Fig. 1(*c*), which are representative of the channel shapes typically used in applications. The elastic medium is treated as a Hookean solid with modulus $E$ and Poisson's ratio $\nu$. Previously it was shown that theoretical predictions based on Hooke's law are in strong agreement with experimental measurements for microchannels with rectangular [18] and triangular [20] cross section. The field equations and numerical solution method are presented in Sec. 2 along with exact and approximate analytic solutions based on classical solutions from the theory of linear elasticity. The numerical, exact, and approximate solutions are compared in Sec. 3 and shown to be in good agreement. This is followed by a discussion of how the proposed model can inform the design of selected systems. The paper closes with a brief summary of the results and prospects for future progress within the still nascent field of soft microfluidic mechanics and modeling (Sec. 4).

## 2 Theory

A rectangular elastic sheet of dimensions $\{L_1, L_2, L_3\}$ is embedded with a single microchannel of width $w$ and height $h$ that extends along its entire depth. Referring to the coordinates in Fig. 1(*b*), the sheet is subject to compressive pressure $p$ on its top ($X_2 = L_2/2$) and bottom ($X_2 = -L_2/2$) surfaces. This induces a displacement field $\mathbf{u} = u_i(\mathbf{X})\mathbf{E}_i$ and stress $\boldsymbol{\sigma} = \sigma_{ij}(\mathbf{X})\mathbf{E}_i \otimes \mathbf{E}_j$ within the elastomer. Here, $\mathbf{X} = X_i\mathbf{E}_i \in \mathcal{B}_0$, $\mathcal{B}_0$ is the natural placement of the elastic medium in Euclidean space ($\mathcal{E}$), and the indices $i, j \in \{1, 2, 3\}$ are subject to Einstein summation convention. Assuming plane strain loading, $\boldsymbol{\sigma}$ has components [24]

$$\sigma_{11} = \frac{E\{(1-\nu)u_{1,1} + \nu u_{2,2}\}}{(1+\nu)(1-2\nu)} \quad \sigma_{12} = \sigma_{21} = \frac{E(u_{1,2} + u_{2,1})}{2(1+\nu)}$$
$$\sigma_{22} = \frac{E\{\nu u_{1,1} + (1-\nu)u_{2,2}\}}{(1+\nu)(1-2\nu)} \quad \sigma_{33} = \frac{E\nu(u_{1,1} + u_{2,2})}{(1+\nu)(1-2\nu)} \tag{1}$$

$\sigma_{31} = \sigma_{13} = \sigma_{32} = \sigma_{23} = 0$. Here, the notation $f_{,i} = \partial f/\partial X_i$ applies to functions $f : \mathcal{B}_0 \to \mathbb{R}$.

[1]Present address: Laboratory of Intelligent Systems, École Polytechnique Fédérale de Lausanne, Lausanne 1015, Vaud, Switzerland.
[2]Corresponding author.
Contributed by the Applied Mechanics Division of ASME for publication in the Journal of Applied Mechanics. Manuscript received April 29, 2018; final manuscript received May 30, 2018; published online June 27, 2018. Assoc. Editor: Yihui Zhang.

  

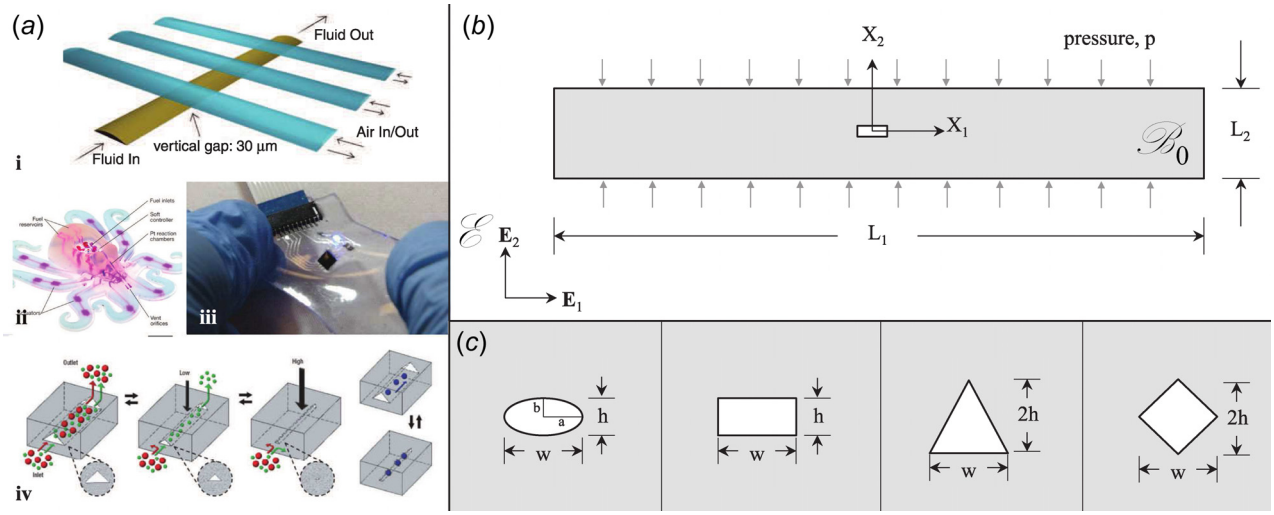


**Fig. 1 (*a*) Examples of soft microfluidics for emerging applications: (*i*) Quake valve (reproduced with permission from Unger et al. [16] Copyright 2000 by AAAS), (*ii*) fluidic soft robot (reproduced with permission from Wehner et al. [14] Copyright 2016 by Springer Nature), (*iii*) LM electronics (reproduced with permission from Ozutemiz et al. [23] Copyright 2018 by Wiley—VCH Verlag GmbH & Co. KGaA), and (*iv*) tunable nanoparticle filtration (reproduced with permission from Huh et al. [21] Copyright 2007 by Springer Nature). (*b*) Soft microfluidic channel modeled as a prismatic opening embedded inside of an elastic sheet subject to surface pressure *p*. (*c*) Selected channel cross section, which is representative of geometries typically used in soft microfluidics.**

For a linear elastic solid, $\mathbf{\nabla}\cdot\boldsymbol{\sigma}=0$ at static equilibrium, where $\mathbf{\nabla}=\{\partial/\partial X_i\}\mathbf{E}_i$ is the Lagrangian (material) nabla operator.[3] Letting $\psi=(1-2\nu)/2(1-\nu)$ and $\nu_1=\nu/(1-\nu)$, it follows from Eq. (1) that the balance law can be expressed by the following pair of partial differential equations:

$$\begin{aligned} u_{1,11}+\nu_1 u_{2,21}+\psi(u_{1,22}+u_{2,12})&=0\\ u_{2,22}+\nu_1 u_{1,12}+\psi(u_{1,21}+u_{2,11})&=0 \end{aligned} \tag{2}$$

The solution to this displacement formulation[4] must satisfy the following boundary conditions:

$$\boldsymbol{\sigma}\cdot\mathbf{n}=\mathbf{t}\ \ \forall\mathbf{X}\in\partial\mathcal{B}_0'\quad \boldsymbol{\sigma}\cdot\mathbf{n}=0\ \ \forall\mathbf{X}\in\partial\mathcal{B}_0\backslash\partial\mathcal{B}_0' \tag{3}$$

Here, $\mathcal{B}_0'$ corresponds to the top and bottom surfaces ($X_2=\pm L_2/2$) and $\mathbf{t}$ is the prescribed surface traction. In component form, $\mathbf{t}=\mp p\mathbf{E}_2$ on $X_2=\pm L_2/2$.

**2.1 Numerical Solution.** A numerical solution to the above boundary value problem is obtained in MATLAB R2015a (The Mathworks, Inc., Natick, MA) using the *pdenonlin* function. This solver uses the method of finite elements in which the domain $\mathcal{B}_0$ is converted to a triangular mesh. The finite element matrices are then generated on the mesh and solved using a damped Gauss-Newton iteration algorithm. Numerical solutions are obtained for thin sheets with $\nu=0.49$ (i.e., incompressible) and unitless dimensions $L_1=10$ and $L_2=1$ and channels of width $w=0.1$ and height $h$ ranging from 0.01 to 0.1. If units of millimeters are selected, then the selected values are representative of typical microfluidic systems.

The governing equations in (2) are imported into *pdenonlin* as a system of elliptic partial differential equations with the general form

$$\nabla\cdot(\mathbf{C}:\nabla\mathbf{u})=\mathbf{a}\mathbf{u}+\mathbf{f} \tag{4}$$

where $\mathbf{C}$, $\mathbf{a}$, and $\mathbf{f}$ are fourth-, second-, and first-order tensors, respectively. For the current problem, $\nabla=(\partial/\partial X_1)\mathbf{E}_1+(\partial/\partial X_2)\mathbf{E}_2$, $\mathbf{a}=\mathbf{f}=\mathbf{0}$, and $\mathbf{C}=C_{ijkl}\mathbf{E}_i\otimes\mathbf{E}_j\otimes\mathbf{E}_k\otimes\mathbf{E}_l$. From Eq. (2), it follows that

$$\begin{aligned} C_{1111}&=C_{2222}=1 \qquad C_{1122}=C_{2211}=\nu_1\\ C_{1212}&=C_{1221}=C_{2112}=C_{2121}=\psi \end{aligned} \tag{5}$$

and the remaining elements of $\mathbf{C}$ are zero. In MATLAB, $\mathbf{C}$ is imported as a column vector of character strings with elements (1, 0, 0, $\psi$, 0, $\psi$, $\nu_1$, 0, 0, $\nu_1$, $\psi$, 0, $\psi$, 0, 0, 1). Likewise, the boundary conditions in Eq. (3) must be expressed as

$$(\mathbf{C}:\nabla\mathbf{u})\cdot\mathbf{n}+\mathbf{q}\mathbf{u}=\mathbf{g} \tag{6}$$

where $\mathbf{q}$ is a second-order tensor and $\mathbf{g}$ is the prescribed surface traction. Here, $\mathbf{q}=\mathbf{0}$ and

$$\mathbf{g}=\begin{cases}\hat{\mathbf{t}} & \forall\mathbf{X}\in\partial\mathcal{B}_0'\\ 0 & \forall\mathbf{X}\in\partial\mathcal{B}_0\backslash\partial\mathcal{B}_0'\end{cases} \tag{7}$$

where the nondimensional traction can be expressed as

$$\hat{\mathbf{t}}=\mp\frac{(1+\nu)(1-2\nu)p}{(1-\nu)E}\mathbf{E}_2 \tag{8}$$

for $X_2=\pm L_2/2$. For convenience, we will also define a normalized surface pressure $\hat{p}=p/E$. As shown next, the normalized surface pressure $\hat{p}$ will also be useful in calculating the *gauge factor* that relates applied pressure with the change in cross-sectional area $\Delta A$ of the microchannel.

The cross-sectional area of the microchannel is determined by using Green's theorem

$$A=\frac{1}{2}\oint_{\mathcal{C}}\{x^c\,dy^c-y^c\,dx^c\} \tag{9}$$

Here, the contour $\mathcal{C}$ represents the space curve formed by the microchannel boundary in the natural placement (undeformed configuration). The coordinates $(x^c, y^c)$ are obtained from the

[3]It should be noted that for problems in which large deformations are anticipated (finite elasticity), the elastic medium should be treated as a hyperelastic solid with an internal Cauchy stress that is divergence free in the spatial description, i.e., use the Eulerian nabla operator for $\nabla$.

[4]Also known as Navier's or Lamé's equations.

deformation mapping $\mathbf{x} = \mathbf{X} + \mathbf{u}$ for points $\mathbf{X}^c \in \mathcal{C}$. In parametric form, $X^c_\alpha = X^c_\alpha(t)$ for $\alpha \in \{1, 2\}$, where $t$ can be an arclength along the boundary or angle defined with respect to the $X_1$ axis. The parameter $t$ must increase when moving along $\mathcal{C}$ in the counterclockwise direction.[5] In discrete form where $t$ is an array of length $n$, the contour is discretized by points $x^c_i = (X_1)^c_i + u_1(\mathbf{X}^C_i)$ and $y^c_i = (X_2)^c_i + u_2(\mathbf{X}^c_i)$, where $(X_\alpha)^c_i = X^c_\alpha(t_i)$ and $i \in \{1,\ldots, n\}$. The area is calculated as

$$A = \frac{1}{2}\sum_{i=2}^{n}\{x^c_i\,\Delta y^c_i - y^c_i\,\Delta x^c_i\} \tag{10}$$

where $\Delta x^c_i = x^c_i - x^c_{i-1}$ and $\Delta y^c_i = y^c_i - y^c_{i-1}$. Finally, the gauge factor corresponds to the ratio of the relative change in cross-sectional area $\Delta A/A_0$ and normalized pressure

$$\mathcal{G} = \lim_{p\to 0}\frac{1}{\hat{p}}\left\{1 - \frac{A}{A_0}\right\} \tag{11}$$

In soft microfluidics, the parameter $\mathcal{G}$ is an important metric for elasto-mechanical coupling that relates the "sensitivity" of the microchannel geometry to an applied surface traction.

**2.2 Analytic Solution.** As with other classes of problems in two-dimensional (2D) linear elasticity, an analytic solution to the above boundary value problem can be obtained using complex analysis. This involves replacing the coordinates $(x_1, x_2)$ within the elastic media by a complex variable, $z = x_1 + ix_2$. Using the Kolosov-Muskhelishvili formulae [24,25], the stress and displacement fields can be expressed in terms of analytic complex stress potential functions $\phi(z)$, $\psi(z)$

$$\begin{aligned}\sigma_{11} + \sigma_{22} &= 2[\phi_1'(z) + \overline{\phi_1'(z)}]\\ \sigma_{22} - \sigma_{11} + 2i\sigma_{12} &= 2[\bar{z}\phi_1''(z) + \psi_1'(z)]\\ 2\mu(u_1 + iu_2) &= \kappa\phi(z) - z\overline{\phi'(z)} - \overline{\psi(z)}\end{aligned} \tag{12}$$

where $\kappa = 3 - 4\nu$; $\bar{z}$, $\overline{\phi(z)}$, and $\overline{\psi(z)}$ are the complex conjugates of $z$, $\phi(z)$, and $\psi(z)$, respectively. The prime in Eq. (12) denotes the derivative with respect to $z$.

To find the displacement field around holes in an infinite media, a conformal transformation $z = \omega(\zeta)$, is employed to map the region in $\mathcal{B}_0$ outside the hole, from the $z$ plane to the interior of a unit circle in the $\zeta$ plane

$$2\mu(u_1 + iu_2) = \kappa\phi(\zeta) - \frac{\omega(\zeta)}{\overline{\omega'(\zeta)}}\overline{\phi'(\zeta)} - \overline{\psi(\zeta)} \tag{13}$$

where $\psi(\zeta) = \psi\circ\omega(\zeta)$ and $\phi(\zeta) = \phi\circ\omega(\zeta)$. The mapping function $\omega(\zeta)$ takes the general form [26]

$$\omega(\zeta) = R\left[\frac{1}{\zeta} + \sum_{k=1}^{\infty} m_k\zeta^{2k-1}\right] \tag{14}$$

Here, $R$ is a scaling factor that depends upon the dimensions of the hole geometry. Since the series in Eq. (14) converges rapidly, we truncate the expression to three terms. For an ellipse of dimensions $(a, b)$, $m_1 = (a-b)/(a+b)$, $m_2 = 0$, $m_3 = 0$, and for a rectangle of dimensions $(w, h)$, $m_1 = (a+\overline{a})/2$, $m_2 = (a-\overline{a})^2/24$, $m_3 = \{(a^2-\overline{a}^2)(a-\overline{a})\}/80$, where $a = e^{2ik\pi}$ and $k = 0.068\log(38.314\cdot h/w)$.

As reported in Ref. [25], the stress potential functions $\{\phi(\zeta), \psi(\zeta)\}$ can each be resolved into the pair of functions

$$\begin{aligned}\phi_1(\zeta) &= \frac{p\,\omega(\zeta)}{4}\\ \psi_1(\zeta) &= \frac{p\,\omega(\zeta)}{2}\end{aligned} \tag{15}$$

and the following pair of holomorphic functions in the region $|\zeta| < 1$:

$$\begin{aligned}\phi_0(\zeta) &= \sum_{n=1}^{\infty} a_n\zeta^n\\ \psi_0(\zeta) &= \sum_{n=0}^{\infty} b_n\zeta^n\end{aligned} \tag{16}$$

The expressions for $\phi(\zeta)$ and $\psi(\zeta)$ are found by applying Cauchy integrals to the derived boundary conditions on the contour $\gamma$ of the fictitious hole in the parametric $\zeta$-plane and solving the resulting pair of equations [27]

$$\begin{aligned}\phi_0(\zeta) + \frac{1}{2\pi i}\int_\gamma \frac{\omega(\sigma)}{\overline{\omega'(\sigma)}}\frac{\overline{\phi_0'(\sigma)}}{\sigma-\zeta}d\sigma &= \frac{1}{2\pi i}\int_\gamma \frac{f_1^0 + if_2^0}{\sigma-\zeta}d\sigma\\ \psi_0(\zeta) + \frac{1}{2\pi i}\int_\gamma \frac{\overline{\omega(\sigma)}}{\omega'(\sigma)}\frac{\phi_0'(\sigma)}{\sigma-\zeta}d\sigma &= \frac{1}{2\pi i}\int_\gamma \frac{f_1^0 - if_2^0}{\sigma-\zeta}d\sigma\end{aligned} \tag{17}$$

The derived boundary conditions for the basic stress state of this medium are [25]

$$\begin{aligned}f_1^0 + if_2^0 &= \frac{pR}{2}\left[\omega(\zeta) + \overline{\omega(\zeta)}\right]\\ f_1^0 - if_2^0 &= \frac{pR}{2}\left[\overline{\omega(\zeta)} + \omega(\zeta)\right]\end{aligned} \tag{18}$$

As an example, the stress potential functions for an ellipse $\{\phi_e(\zeta), \psi_e(\zeta)\}$ and a rectangle $\{\phi_r(\zeta), \psi_r(\zeta)\}$ of aspect ratio $h/w = b/a = 0.5$ are given by

$$\begin{aligned}\phi_e(\zeta) &= \hat{p}R\left(\frac{1}{4\zeta} - 0.583\zeta\right)\\ \psi_e(\zeta) &= \hat{p}R\left(\frac{1}{2\zeta} + 1.5\zeta + \frac{6.67\zeta}{\zeta^2 - 3}\right)\end{aligned} \tag{19}$$

and

$$\begin{aligned}\phi_r(\zeta) &= \hat{p}R\left(\frac{1}{4\zeta} - 0.486\zeta + 0.0382\zeta^3\right)\\ \psi_r(\zeta) &= \hat{p}R\left(\frac{1}{2\zeta} - \frac{0.773\zeta^3 + 1.332\zeta}{0.918\zeta^4 - 0.574\zeta^2 + 2}\right)\end{aligned} \tag{20}$$

respectively. The equations in (19) match those provided in previous studies [28].

Finally, the displacement field is obtained by substituting Eqs. (14), (19), and (20) into Eq. (13). The area of the hole is numerically determined by importing the vector of contour points into the *polyarea* function in MATLAB 2016b. The gauge factor is calculated by $\mathcal{G} = (1 - A/A_0)/\hat{p}$. As discussed in Sec. 3, the values of $A/A_0$ and $\mathcal{G}$ are plotted in Figs. 2 and 3 and compared with the numerical and approximate analytic solutions.

**2.3 Approximate Solution.** The displacement field $\mathbf{u} : \mathcal{B}_0 \to \mathcal{B}$, microchannel area $A$, and gauge factor $\mathcal{G}$ can be approximated by adapting solutions from classical problems in linear elasticity. As shown in Sec. 3, these closed-form approximations are found to be in reasonable agreement with the numerical and exact analytic solutions and can be useful for establishing design and operational guidelines for soft microfluidic systems.

*2.3.1 Elliptical Cross Section.* We begin with the deformation of the elliptical cross section shown in Fig. 1(*c*). This can be determined by first examining the deformation of a circular cross section of radius $R_0$ under pressure $p_0$ such that the channel deforms into an ellipse with principle axes $a$ and $b$ (along the $\mathbf{E}_1$ and $\mathbf{E}_2$

[5]Otherwise, the coefficient 1/2 in Eq. (9) should be replaced with –1/2.

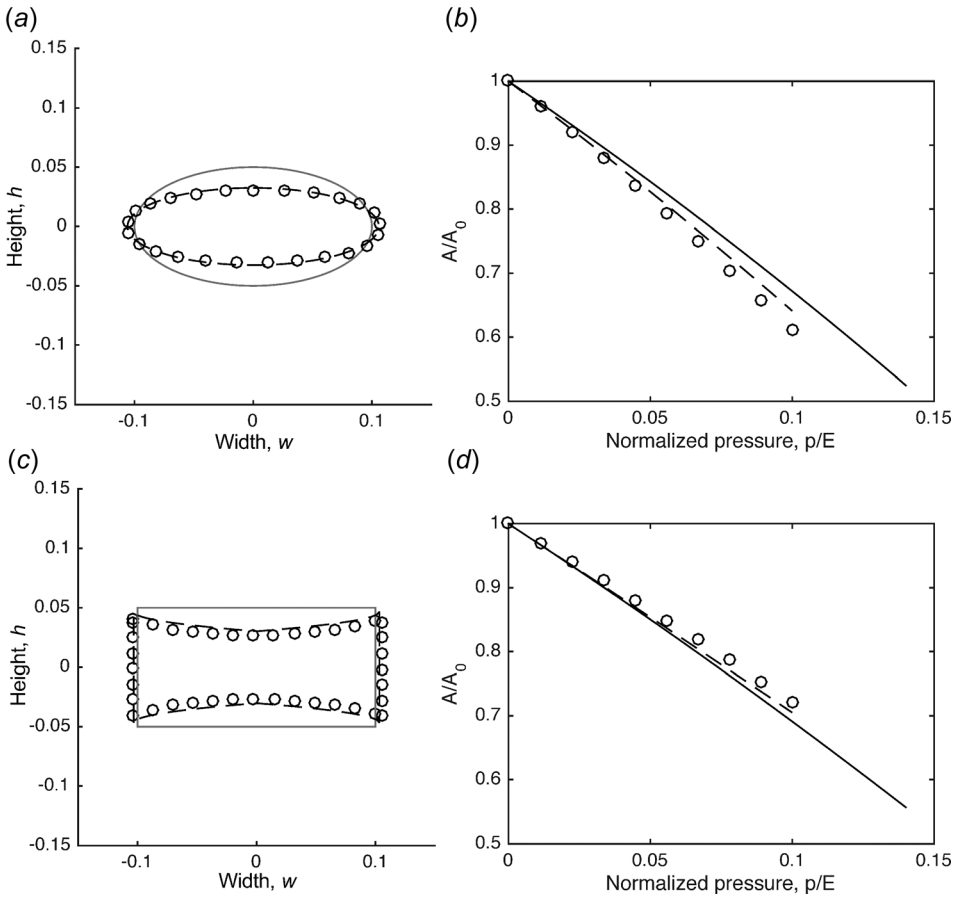


**Fig. 2** (*a*) **Deformation of an elliptical channel with $w = 0.2$, $h = 0.1$, $p = 0.05$, and $\nu = 0.49$: (gray) initial shape, (markers) numerical solution for deformed shape, (dashed) approximate solution for deformed shape. (*b*) Cross-sectional area as a function of normalized pressure: (circular markers) numerical solution, (dashed) approximate solution, and (solid) analytic solution. (*c*) Deformation of a rectangular channel with $w = 0.2$, $h = 0.1$, $p = 0.05$, and $\nu = 0.49$: (gray) initial shape, (markers) numerical solution for deformed shape, (dashed) approximate solution for deformed shape. (*d*) Cross-sectional area as a function of normalized pressure: (circular markers) numerical solution, (dashed) approximate solution, and (solid) analytic solution.**

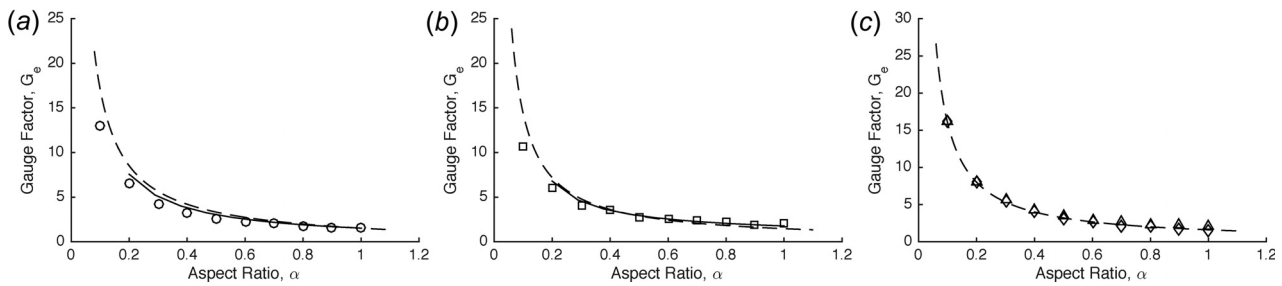


**Fig. 3 Gauge factor $\mathcal{G}$ versus channel aspect ratio $\alpha$. (*a*) Circular cross section with $a = 0.1$ and varying $b$: (circular markers) numerical solution, (solid) analytic solution, (dashed) approximate solution. (*b*) Rectangular cross section with $w = 0.1$ and varying $h$: (square markers) numerical solution, (solid) analytic solution, and (dashed) approximate solution. (*c*) Numerical solutions for triangular (triangle markers) and diamond-shape (diamond markers) also exhibit a similar monotonic dependency; the dashed line corresponds to a fit of $\mathcal{G} = 1.2/\alpha$.**

directions, respectively). By linear superposition, the deformation of this ellipse under a surface traction $p$ is equal to the deformation of a circular channel of radius $R_0$ subject to an applied pressure of $p' = p_0 + p$. Referring to Fig. 4, this corresponds to selecting different configurations for the natural ($\mathcal{B}_0'$) and reference placements ($\mathcal{B}_0$) and decomposing the deformation mapping $\chi' = \chi \circ \chi_0$ into an intermediate mapping $\chi_0 : \mathcal{B}_0' \to \mathcal{B}_0$ and final mapping $\chi : \mathcal{B}_0 \to \mathcal{B}$.

Study of the deformation of a circular hole in an elastic medium with far-field uniaxial stress is classically known as the *Michell problem* [24,25]. For a compressive stress $p_0$, the displacement field around the hole boundary has components

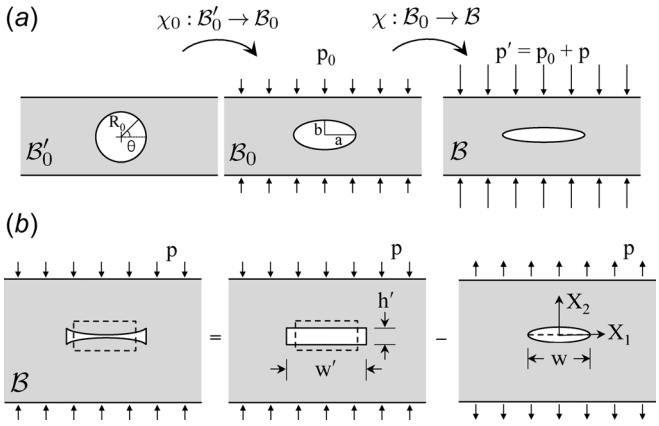


**Fig. 4 (*a*) The solution to the classical *Michell* problem of a circular opening in an elastic plate under far-field stress is used to estimate the deformation of an elliptical channel with principle dimensions *a* and *b*. (*b*) The deformation of a rectangular channel is estimated by superposing uniform deformation of a homogenous Hookean solid with the opening of a slit under far-field stress.**

$$u_1(\theta) = \frac{2(1+\nu)}{E}\varphi p_0 R_0 \cos\theta \tag{21}$$

$$u_2(\theta) = -\frac{6(1+\nu)}{E}\varphi p_0 R_0 \sin\theta \tag{22}$$

where $\varphi = (k+1)/8$, $k = 3-4\nu$, and the polar coordinate $\theta$ is defined with respect to the $X_1$ axis. To achieve an elliptic cross section with dimensions $a = w/2$ and $b = h/2$, the elastic medium must be deformed such that $u_1(0) = a - R_0$ and $u_2(\pi/2) = b - R_0$. This implies the following opening radius and surface pressure:

$$p_0 = \frac{E(1-\alpha)}{2\varphi(1+\nu)(3+\alpha)} \tag{23}$$

$$R_0 = \frac{w}{2}\left\{1 + \frac{2(1+\nu)\varphi p_0}{E}\right\}^{-1} \tag{24}$$

where $\alpha = h/w$ is the aspect ratio.

The final shape of the channel is determined by superposition

$$x_1^c = R_0 \cos\theta\left\{1 + \frac{2\varphi(1+\nu)(p+p_0)}{E}\right\} \tag{25}$$

$$x_2^c = R_0 \sin\theta\left\{1 - \frac{6\varphi(1+\nu)(p+p_0)}{E}\right\} \tag{26}$$

The corresponding cross-sectional area is

$$A = \pi R_0^2\left\{1 + \frac{2\varphi(1+\nu)(p+p_0)}{E}\right\}\left\{1 - \frac{6\varphi(1+\nu)(p+p_0)}{E}\right\} \tag{27}$$

and the gauge factor is $\mathcal{G}_e = (1-\nu^2)(9-\alpha^2)/4\alpha$. As would be expected for a relatively small channel in a large linear elastic medium, resistance to deformation under a normalized pressure $p/E$ decreases with an increase in the height-to-width aspect ratio of the cross section.

*2.3.2 Rectangular Cross Section.* For a rectangular cross section, closed-form algebraic approximations for $A/A_0$ and $\mathcal{G}$ can be obtained by examining the dual case of tensile loading. Under tension, the final area can be estimated by superposing the area $A_\varepsilon = wh(1+\varepsilon)(1-\nu(1+\nu)\varepsilon)$ under a uniform global (average) strain $\varepsilon = \sigma(1-\nu^2)/E$ with the increase in area ($\Delta A$) for a *crack opening* under a far-field tension $\sigma$. The latter is obtained from linear elastic fracture mechanics, by treating the channel cross section as a narrow slit of width $w$. Referring to Fig. 4, the vertical displacement of the slit boundary ($u_2$) is obtained for a stress intensity factor $K_I = \sigma\sqrt{\pi w/2}$ [24,29,30]

$$u_2 = \frac{4(1-\nu^2)K_I}{E}\sqrt{\frac{w-2X_1}{4\pi}} \tag{28}$$

Integrating over the length of the slit yields $\Delta A = 4(1-\nu^2)\sqrt{2}\sigma w^2/3E$. For compression, $\sigma$ is replaced with $-p$ and the position of points along the boundary is estimated as

$$\mathbf{x}^c = \left(1 + \nu(1+\nu)\frac{p}{E}\right)X_1^c\mathbf{E}_1 + \left\{\left(1 - (1-\nu^2)\frac{p}{E}\right)X_2^c - \mathrm{sgn}(X_2)\frac{4(1-\nu^2)p\sqrt{w}}{2E}\sqrt{\frac{w}{2} - X_1^c}\right\}\mathbf{E}_2 \tag{29}$$

The final cross-sectional area $A = A_\varepsilon + \Delta A$ is calculated as

$$A = wh\left(1 - (1-\nu^2)\frac{p}{E}\right)\left(1 + \nu(1+\nu)\frac{p}{E}\right) - \frac{4(1-\nu^2)\sqrt{2}pw^2}{3E} \tag{30}$$

and the gauge factor is

$$\mathcal{G}_p = 1 - \nu - 2\nu^2 + \frac{4(1-\nu^2)\sqrt{2}}{3\alpha} \tag{31}$$

Again, the gauge factor decreases monotonically with increasing channel aspect ratio. As $\alpha$ gets large, $\mathcal{G}_p$ converges to $1-\nu-2\nu^2$, which corresponds to the case of uniform strain ($A \approx A_\varepsilon$).

## 3 Results and Discussion

Numerical and analytic solutions for an elliptical cross section are presented in Fig. 2 for the following representative parameters: $L_1 = 10$, $L_2 = 1$, $w = 0.2$, $h = 0.1$, $\nu = 0.49$. Figure 2(*a*) shows deformation under a normalized surface traction $|\hat{t}| = (1-\nu^2)\hat{p} = 0.05$. The dashed lines correspond to the boundary of the unloaded state and the solid line corresponds to the numerical solution for the deformed shape obtained using the steps described in Sec. 2.1. The numerical solution for channel deformation appears to be in good agreement with the analytic approximations, shown as the dash-dot line. As shown in Fig. 2(*b*), there is also a reasonable agreement for calculations of the cross-sectional area as a function of applied pressure ($0 \le \hat{p} \le 0.1$). A comparison for the case of rectangular cross section is presented in Figs. 2(*c*) and 2(*d*).

As shown in Fig. 3, there also appears to be good agreement between numerical and analytic calculations of the gauge factor $\mathcal{G}$. For these plots, $L_1 = 10$, $L_2 = 1$, $\nu = 0.49$, and the channel aspect ratio $\alpha$ ranges from 0.1 to 1. In the case of an elliptical cross section (Fig. 3(*a*)), the agreement appears to be close to exact. Figure 3(*b*) shows that Eq. (31) is in strong agreement with the numerical solution for a rectangular channel. As shown in Fig. 3(*c*), the gauge factor of microchannels with triangular (triangle markers) and diamond-shaped (diamond markers) cross section exhibit a similar monotonic dependency on aspect ratio. This can be accurately captured with the approximation $\mathcal{G} = 1.2/\alpha$, which appears to be in good agreement with the numerical solutions in the range of $\alpha \in [0.1, 1]$.

Both the numerical and analytic solutions are only valid when strain is small and the elastomer can be modeled as a linear elastic solid. For large strains, Hooke's law should be replaced with a

nonlinear constitutive model (Neo-Hookean, Mooney-Rivlin, Ogden) and Cauchy stress should be balanced in the Eulerian description (i.e., $\nabla_E \cdot \boldsymbol{\sigma} = 0$). For some cases, *pdenonlin* can still be used, but only with a tensor $\mathbf{C} = \mathbf{C}(\mathbf{u}, \nabla\mathbf{u})$ that accounts for the stretch and rotation of the material coordinates. Otherwise, a more general finite element analysis (FEA) program is required.

In the current deformation analysis, it is also assumed that the walls of the channel do not make contact or interpenetrate. In general, the channel will collapse as the surface pressure approaches $E$. This is especially true for channels with a low cross-sectional aspect ratio ($\alpha$). For such deformations, analysis should also include a *unilateral constraint* to prevent interpenetration

$$\exists! \, \mathbf{X}_1, \mathbf{X}_2 \in \partial\mathcal{B}_0 \backslash \mathcal{C} : \; \chi(\mathbf{X}_1) \equiv \chi(\mathbf{X}_2) \tag{32}$$

where again, $\chi$ is the deformation mapping. The collapse of soft microfluidic channels under elastomer compression has previously been modeled using commercial FEA packages. This includes rectangular and triangular channels as well as triangular channels embedded with rigid spherical beads. While pressure-induced channel collapse is undesirable for LM circuits and sensors, it is central to the operation of soft microfluidic valves and particle filtration networks.

Hydrostatic pressure ($p_h$) within the microfluidic channel can typically be ignored when surface pressure is concentrated over a small portion of the channel. For such cases, the reduction in internal volume from localized elastomer deformation is compensated by an equal increase distributed over a much larger volume (away from where pressure is applied). The latter requires only modest tractions on the channel wall and the corresponding hydrostatic pressure is expected to be small compared to the concentrated surface pressure. For cases when $p_h$ is significant, Eq. $(3)_2$ should be replaced with the boundary condition $\boldsymbol{\sigma} \cdot \mathbf{n} = -p_h \mathbf{n} \, \forall \mathbf{X} \in \partial\mathcal{B}_0 \backslash \partial\mathcal{B}_0^t$. Likewise, analytic estimates may be obtained by superposing the approximations above with solutions for the case when traction is only applied on the channel walls.

The theoretical results and approximate models presented here have the potential to inform the choice of materials, designs, and operational conditions for a variety of soft microfluidic systems. In particular, we find that the gauge factor generally ranges from $\sim$1 to 10 for typical cross-sectional geometries. Therefore, in order for soft microfluidic systems to be resistant to collapse under applied pressure, the elastic modulus of the elastomer should be at least 100$\times$ greater than the maximum anticipated pressures. Alternatively, microfluidic channels that are designed to collapse under pressure should be embedded in an elastomer with a modulus that is approximately equal or 1/10th smaller in magnitude. This is especially useful in designing microfluidic channels for sensing, valving, or tunable particle filtration. For example, a circular channel ($a = b$) filled with ionically conductive fluid or liquid metal embedded in an incompressible elastomer has a gauge factor of 1.64. Based on Ohm's law, i.e., $\Delta R/R_0 = (1 + \Delta A/A_0)^{-1} - 1$, this implies that the electrical resistance $R$ will increase by 50% if a pressure $p = 0.2$E is applied.

Finally, although only elastomer sheets with a single channel are modeled, the numerical approach can easily be extended to multiple embedded channels. For the case when channels are sparsely distributed (i.e., center-to-center spacing $\gg$ channel width), the solutions based on single channel deformation are expected to provide a reasonable approximation. This is because the influence of the channel on the internal strain field is highly localized and expected to have only modest influence on the mechanics of neighboring inclusions.

## 4 Conclusion

The compression of microchannels in an elastic medium has important implications in the design and operation of soft microfluidic systems. Of particular interest is the gauge factor $\mathcal{G}$ that relates the relative change in channel area ($\Delta A/A_0$) with the normalized pressure ($p/E$) exerted on the surface of the surrounding elastomer. For the case of rectangular and elliptical cross section, there is good agreement between closed-form analytic approximations based on classical solutions in 2D elasticity with numerical solutions to the governing Lamé equations. In the case of a pressure-controlled microfluidic valve, filter, or sensor, the approximations can be useful for selecting material stiffness and channel aspect ratio for an anticipated range of pressures.

The numerical method presented here is applicable for examining small deformation of any prismatic channel geometry, including triangle, diamond, and other polygon-shaped cross section. For larger deformations, the theory must be modified to account for finite elastic deformation and unilateral contact between channel walls (i.e., collapse). Three-dimensional FEA modeling is required for accurate modeling of more general microfluidic networks with multiple channels and nonprismatic geometries. However, even for these general systems, the approximations presented here can help guide channel design and materials selection.


## Acknowledgment

This work was supported by an Office of Naval Research BRC (Bio-Inspired Autonomous Systems, Dr. Tom McKenna).

## Funding Data

- Office of Naval Research (N00014-7-1-2063).


## References


[1] Stone, H. A., Stroock, A. D., and Ajdari, A., 2004, "Engineering Flows in Small Devices: Microfluidics Toward a Lab-on-a-Chip," Annu. Rev. Fluid Mech., **36**(1), pp. 381–411.

[2] Squires, T. M., and Quake, S. R., 2005, "Microfluidics: Fluid Physics at the Nanoliter Scale," Rev. Mod. Phys., **77**(3), p. 977.

[3] Whitesides, G. M., 2006, "The Origins and the Future of Microfluidics," Nature, **442**(7101), pp. 368–373.

[4] Sackmann, E. K., Fulton, A. L., and Beebe, D. J., 2014, "The Present and Future Role of Microfluidics in Biomedical Research," Nature, **507**(7491), pp. 181–189.

[5] Xia, Y., and Whitesides, G. M., 1998, "Soft Lithography," Annu. Rev. Mater. Sci., **28**(1), pp. 153–184.

[6] Quake, S. R., and Scherer, A., 2000, "From Micro-to Nanofabrication With Soft Materials," Science, **290**(5496), pp. 1536–1540.

[7] Qin, D., Xia, Y., and Whitesides, G. M., 2010, "Soft Lithography for Micro-and Nanoscale Patterning," Nat. Protoc., **5**(3), pp. 491–502.

[8] Dickey, M. D., Chiechi, R. C., Larsen, R. J., Weiss, E. A., Weitz, D. A., and Whitesides, G. M., 2008, "Eutectic Gallium-Indium (Egain): A Liquid Metal Alloy for the Formation of Stable Structures in Microchannels at Room Temperature," Adv. Funct. Mater., **18**(7), pp. 1097–1104.

[9] Cheng, S., and Wu, Z., 2012, "Microfluidic Electronics," Lab Chip, **12**(16), pp. 2782–2791.

[10] Joshipura, I. D., Ayers, H. R., Majidi, C., and Dickey, M. D., 2015, "Methods to Pattern Liquid Metals," J. Mater. Chem. C, **3**(16), pp. 3834–3841.

[11] Huh, D., Kim, H. J., Fraser, J. P., Shea, D. E., Khan, M., Bahinski, A., Hamilton, G. A., and Ingber, D. E., 2013, "Microfabrication of Human Organs-on-Chips," Nat. Protoc., **8**(11), pp. 2135–2157.

[12] Bhatia, S. N., and Ingber, D. E., 2014, "Microfluidic Organs-on-Chips," Nat. Biotechnol., **32**, pp. 760–772.

[13] Wakimoto, S., Ogura, K., Suzumori, K., and Nishioka, Y., 2009, "Miniature Soft Hand With Curling Rubber Pneumatic Actuators," IEEE International Conference on Robotics and Automation (ICRA'09), Kobe, Japan, May 12–17, pp. 556–561.

[14] Wehner, M., Truby, R. L., Fitzgerald, D. J., Mosadegh, B., Whitesides, G. M., Lewis, J. A., and Wood, R. J., 2016, "An Integrated Design and Fabrication Strategy for Entirely Soft, Autonomous Robots," Nature, **536**(7617), pp. 451–455.

[15] Kim, H.-J., Son, C., and Ziaie, B., 2008, "A Multiaxial Stretchable Interconnect Using Liquid-Alloy-Filled Elastomeric Microchannels," Appl. Phys. Lett., **92**(1), p. 011904.

[16] Unger, M. A., Chou, H.-P., Thorsen, T., Scherer, A., and Quake, S. R., 2000, "Monolithic Microfabricated Valves and Pumps by Multilayer Soft Lithography," Science, **288**(5463), pp. 113–116.

[17] Whitney, R., 1949, "The Measurement of Changes in Human Limb-Volume by Means of a Mercury-Inrubber Strain Gauge," J. Physiol., **109**(1–2), p. Proc–5.

[18] Majidi, C., Park, Y.-L., Kramer, R., Bérard, P., and Wood, R. J., 2010, "Hyperelastic Pressure Sensing With a Liquid-Embedded Elastomer," J. Micromech. Microeng., **20**(12), p. 125029.

[19] Park, Y.-L., Tepayotl-Ramirez, D., Wood, R. J., and Majidi, C., 2012, "Influence of Cross-Sectional Geometry on the Sensitivity and Hysteresis of Liquid-Phase Electronic Pressure Sensors," Appl. Phys. Lett., **101**(19), p. 191904.

[20] Tepáyotl-Ramírez, D., Lu, T., Park, Y.-L., and Majidi, C., 2013, "Collapse of Triangular Channels in a Soft Elastomer," Appl. Phys. Lett., **102**(4), p. 044102.
[21] Huh, D., Mills, K., Zhu, X., Burns, M. A., Thouless, M., and Takayama, S., 2007, "Tuneable Elastomeric Nanochannels for Nanofluidic Manipulation," Nat. Mater., **6**(6), pp. 424–428.
[22] Sparreboom, W., Van Den Berg, A., and Eijkel, J., 2009, "Principles and Applications of Nanofluidic Transport," Nat. Nanotechnol., **4**(11), pp. 713–720.
[23] Ozutemiz, K. B., Wissman, J., Ozdoganlar, O. B., and Majidi, C., 2018, "Egain–Metal Interfacing for Liquid Metal Circuitry and Microelectronics Integration," Adv. Mater. Interfaces, **5**(10), p. 1701596.
[24] Sadd, M. H., 2009, *Elasticity: Theory, Applications, and Numerics*, 2nd ed., Academic Press, Waltham, MA.
[25] Muskhelishvili, N. I., 1977, *Some Basic Problems of the Mathematical Theory of Elasticity*, 1st ed., Springer, Berlin.
[26] Smirnov, V. I., 1964, *A Course of Higher Mathematics*, Vol. 5, Elsevier, Oxford, England.
[27] Savin, G. N., 1961, *Stress Concentration Around Holes*, Vol. 1, Pergamon Press, Oxford, England.
[28] Kachanov, M. L., Shafiro, B., and Tsukrov, I., 2003, *Handbook of Elasticity Solutions*, Springer Science & Business Media, Berlin, Germany.
[29] Anderson, T. L., and Anderson, T., 2005, *Fracture Mechanics: Fundamentals and Applications*, CRC Press, Bacon Raton, FL.
[30] Adams, G. G., 2015, "Critical Value of the Generalized Stress Intensity Factor for a Crack Perpendicular to an Interface," Proc. R. Soc. A, **471**, p. 20150571.